Supplementary Information

Molecular insights into the activation mechanism of GPR156 in maintaining auditory function

Xiangyu Ma, Li-Nan Chen, Menghui Liao, Liyan Zhang, Kun Xi, Jiamin Guo, Cangsong Shen, Dan-Dan Shen, Pengjun Cai, Qingya Shen, Jieyu Qi, Huibing Zhang, Shao-Kun Zang, Ying-Jun Dong, Luwei Miao, Jiao Qin, Su-Yu Ji, Yue Li, Jianfeng Liu*, Chunyou Mao*, Yan Zhang*, Renjie Chai*

*Corresponding: jfliu@mail.hust.edu.cn (J.L.); maochunyou@zju.edu.cn (C.M.); zhang_yan@zju.edu.cn (Y.Z.); renjiec@seu.edu.cn (R.C.)

The PDF file includes:

Supplementary Figures 1-18
Supplementary Tables 1-6
Unprocessed gels and western blots for Supplementary Fig. 2d and e

Other Supplementary Information for this manuscript include the following:

Supplementary Data 1
Source Data

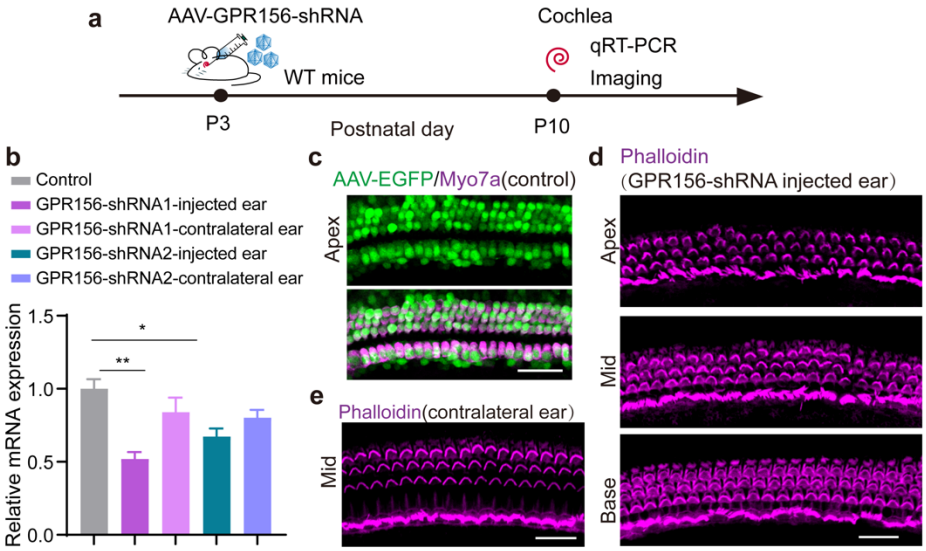

Supplementary Fig. 1 | Knockdown of GPR156 causes a slight deflection of the stereocilia in neonatal mice.

a, The experimental design. AAV dose: 6×10^{10} GC/ear. **b,** The transcriptional expression levels of GPR156 in the apical turn of the GPR156-shRNA-transduced cochlea from 3 independent experiments. *$P < 0.05$, **$P < 0.01$, were calculated by two-tailed unpaired t-test compared to WT mice (mean ± SD (bars), Control vs AAV-GPR156-shRNA1-injected ear: P=0.04946; Control vs AAV-GPR156-shRNA1-contralatearl ear: P=0.255125; Control vs AAV-GPR156-shRNA2-injected ear: P=0.018376; Control vs AAV-GPR156-shRNA2-contralatearl ear: P=0.077506.). Source data are provided as a Source Data file. **c,** Representative images of the control virus infecting inner ear HCs in P3 mice from 6 independent experiments. Scale bar, 40 μm. **d,** Representative confocal images of the stereocilia in the GPR156-shRNA-injected cochlea from 5 independent experiments. Scale bar, 80 μm. **e,** The representative confocal image of stereocilia in the GPR156-shRNA contralateral cochlea from 5 independent experiments. Scale bar, 80 μm.

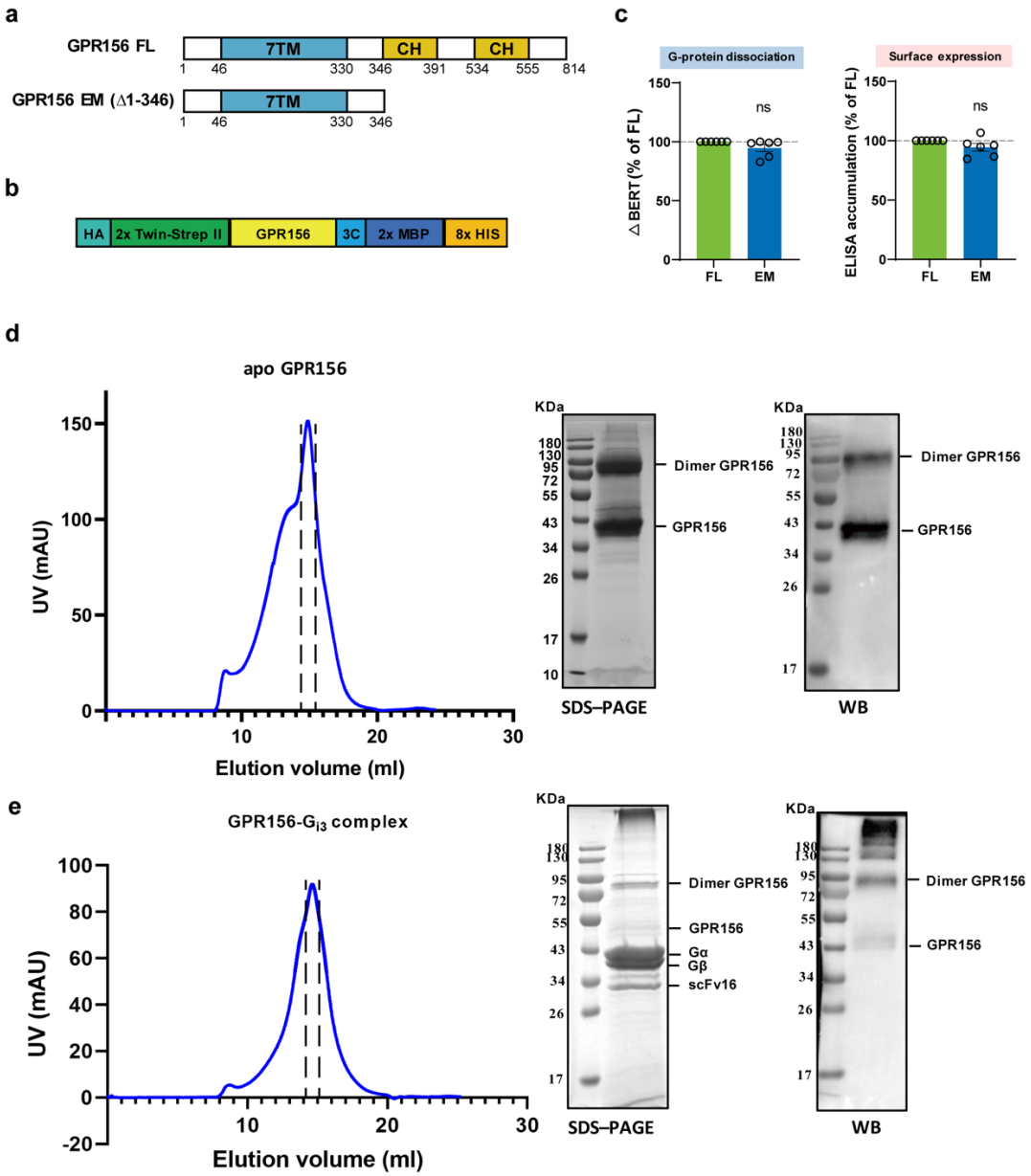

Supplementary Fig. 2 | Optimization and purification of human apo GPR156 and the GPR156–G_{i3} complex.

a, Diagram of the primary structure (FL) of GPR156 domains versus the purification construct (EM). CH: cytoplasmic helices. **b,** Detailed diagram of the purification construct (EM). **c,** Basal activity (left panel) and surface expression (right panel) of the FL and EM constructs of GPR156, as measured by BRET-based assay (from left to right $n = 6, 6$; EM vs FL, P=0.1131) and ELISA assay (from left to right $n = 6, 6$; EM vs FL, P=0.1173), respectively. Data are presented as a percentage of WT activity and are shown as the mean ± SEM (bars) from at least six independent experiments performed in technical triplicate with individual data points shown (dots). ns (not significant) = $P > 0.05$, *$P < 0.05$, **$P < 0.01$, ***$P < 0.001$, ****$P < 0.0001$ by two-tailed unpaired t-test compared to WT. **Supplementary Table 1** provides detailed information. Source data are provided as a Source Data file. **d, e,** Size-exclusion

chromatography profile (left panel), SDS–PAGE gel (middle panel), and western blot (right panel) of the purified apo GPR156 (**d**) and GPR156–G_{i3} complex (**e**). These experiments were repeated three times with similar results. Source data are provided as a Source Data file.

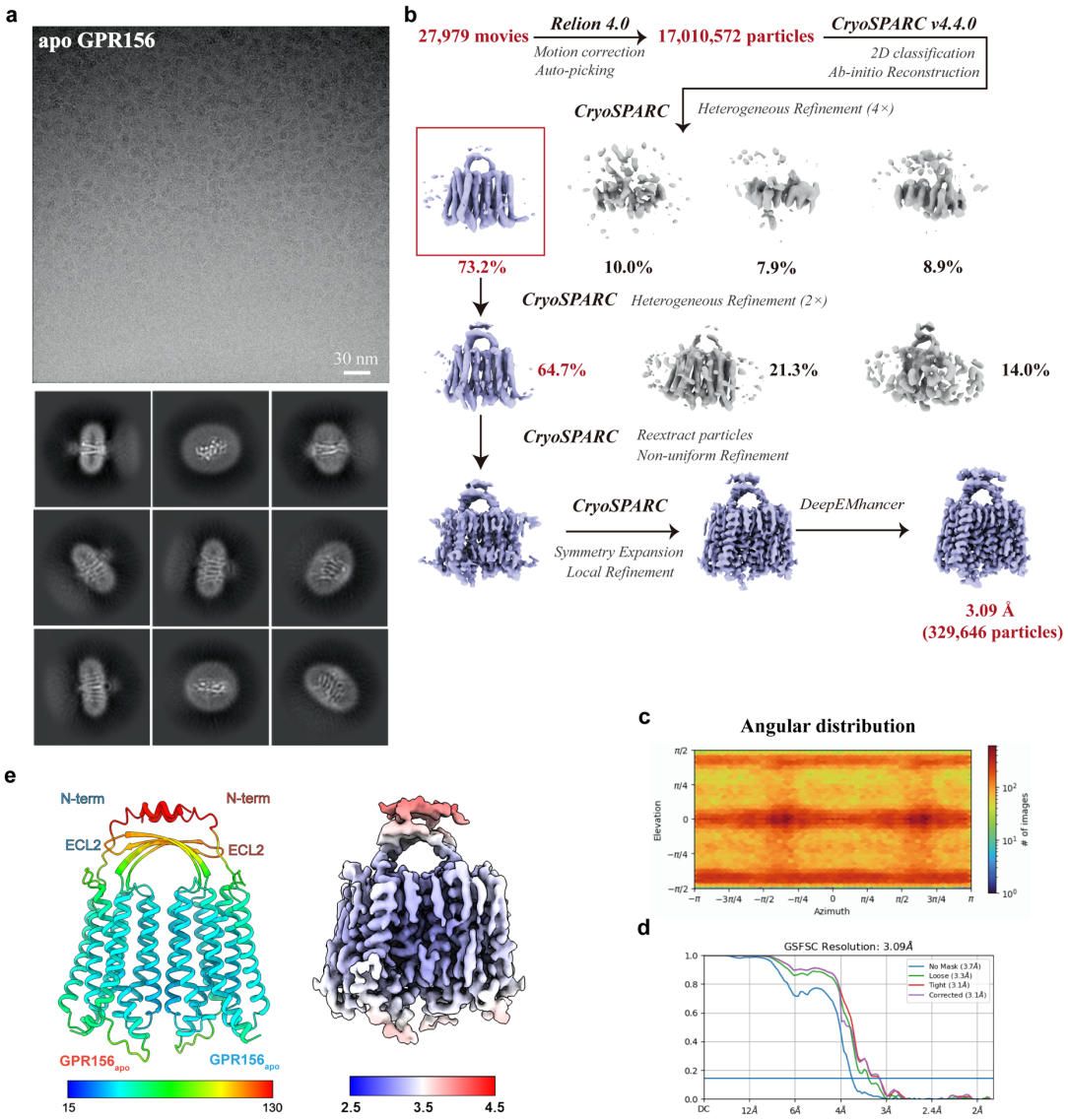

Supplementary Fig. 3 | Workflow of the cryo-EM data processing of apo GPR156.

a, Representative cryo-EM micrograph (top panel) and 2D averages (bottom panel) for apo GPR156. **b,** Cryo-EM data processing workflow for apo GPR156. **c,** Euler angle orientation distribution plots, from CryoSPARC, for the final map of apo GPR156. **d,** No mask fourier shell correlation (FSC) (blue) curve, Corrected (purple), Loose (green), and Tight (red) validation curve of apo GPR156. **e,** Average B-factors plotted on the structure (left panel) and Cryo-EM map colored by local resolution (right panel) of apo GPR156. Blue to red colors indicate lower to higher B-factors and higher to lower map resolution, respectively.

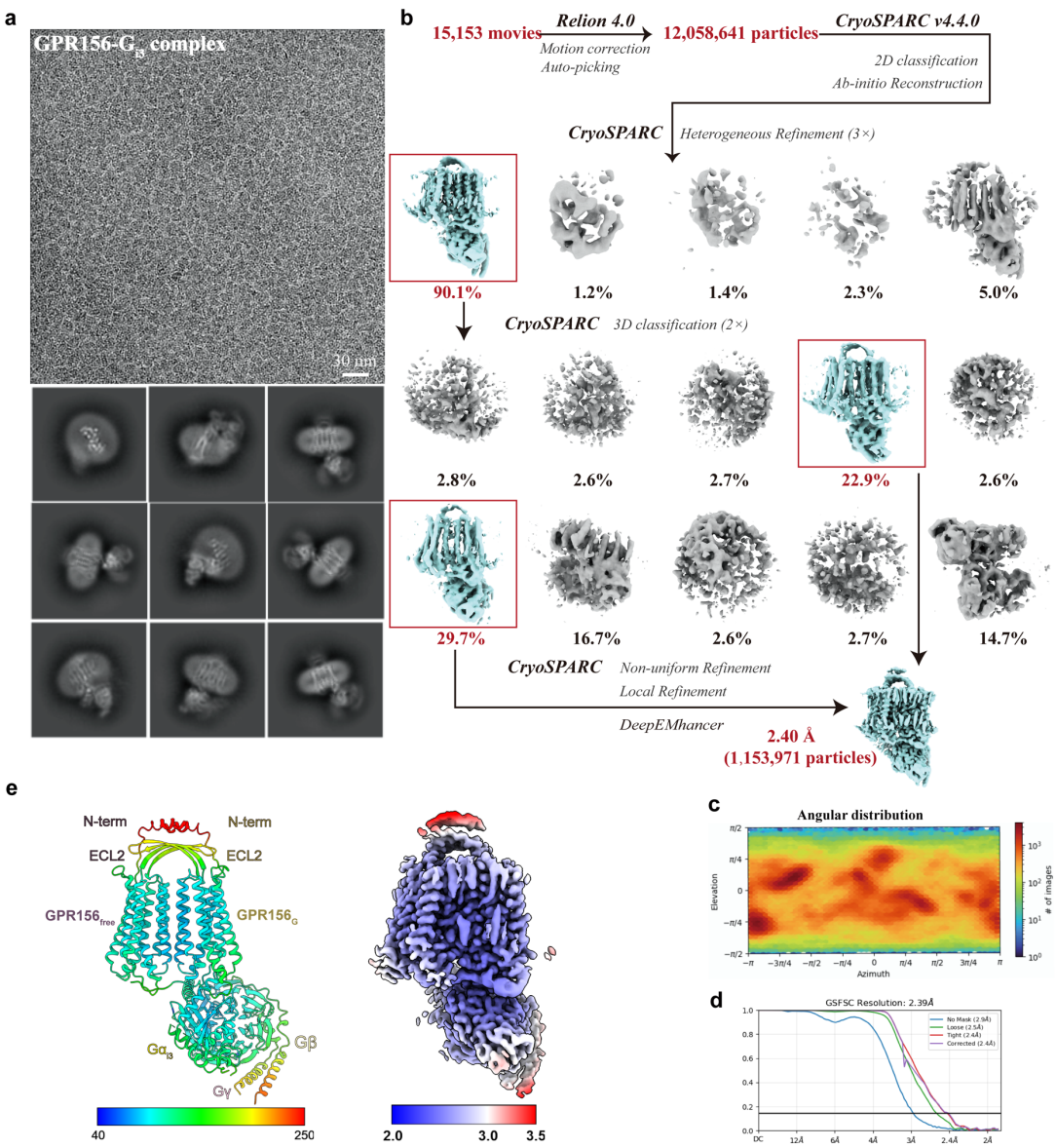

Supplementary Fig. 4 | Workflow of the cryo-EM data processing of the GPR156–G_{i3} complex.

a, Representative cryo-EM micrograph (top panel) and 2D averages (bottom panel) for the GPR156–G_{i3} complex. **b,** Cryo-EM data processing workflow for the GPR156–G_{i3} complex. **c,** Euler angle orientation distribution plots, from CryoSPARC, for the final map of the GPR156–G_{i3} complex. **d,** No mask fourier shell correlation (FSC) (blue) curve, Corrected (purple), Loose (green), and Tight (red) validation curve of the GPR156–G_{i3} complex. **e,** Average B-factors plotted on the structure (left panel) and Cryo-EM map colored by local resolution (right panel) of the GPR156–G_{i3} complex. Blue to red colors indicate lower to higher B-factors and higher to lower map resolution, respectively.

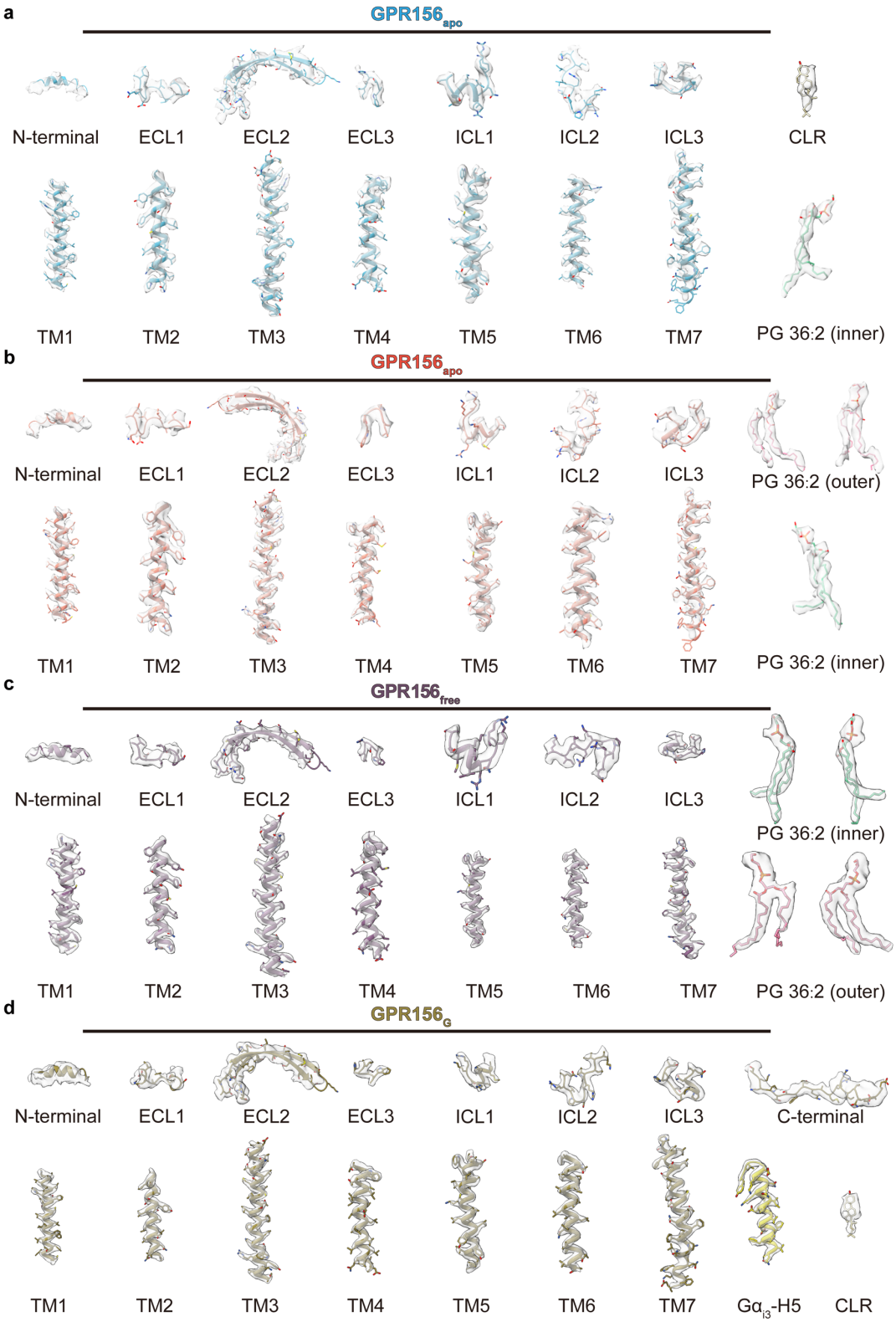

Supplementary Fig. 5 | Structural models of apo GPR156 and the GPR156–G_{i3} complex align with the cryo-EM maps.

a, b, Cryo-EM density and the fitted atomic model for two protomers of apo GRP156, including the N-terminus, transmembrane helices, ECLs, ICLs, CLR, and PG 36:2 inside and outside TMD. **c, d,** Cryo-EM density and the fitted atomic model of the GPR156–G_{i3} complex, including N-terminus, transmembrane helices, ECLs, ICLs,

PG 36:2 of the GPR156 G-free subunit (**c**), N-terminus, transmembrane helices, ECLs, ICLs, CLR, PG 36:2, C-terminus of the GPR156 G-bound subunit, and the α5 helix of $G\alpha_{i3}$ (**d**).

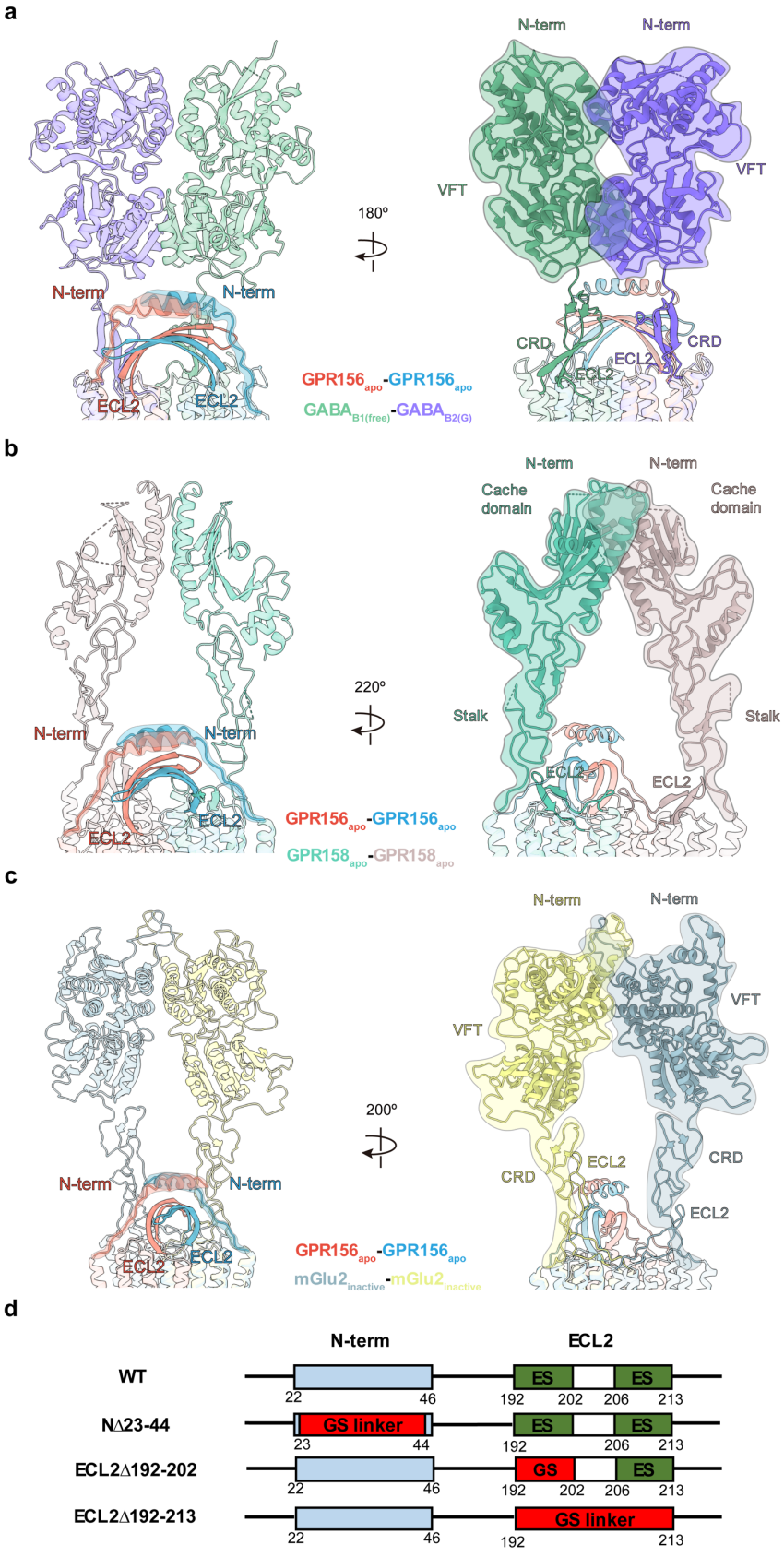

Supplementary Fig. 6 | Comparison of the GPR156 N-terminus and ECL2 with other class C GPCRs.

a-c, Structural comparisons of $GPR156_{apo}$–$GPR156_{apo}$ with $GABA_{B1(free)}$–$GABA_{B2(G)}$ (PDB code: 7EB2) (**a**), $GPR158_{apo}$–$GPR158_{apo}$ (PDB code: 7EWL) (**b**), and $mGlu2_{inactive}$–$mGlu2_{inactive}$ (PDB code: 7EPA) (**c**). **d,** Diagram of the WT GPR156 N-terminus and ECL2 versus the mutant constructs substituted with a GS link (NΔ23–44, ECL2Δ192–213, ECL2Δ192–202). GS link: A linker composed of glycine and serine. ES: β-strand.

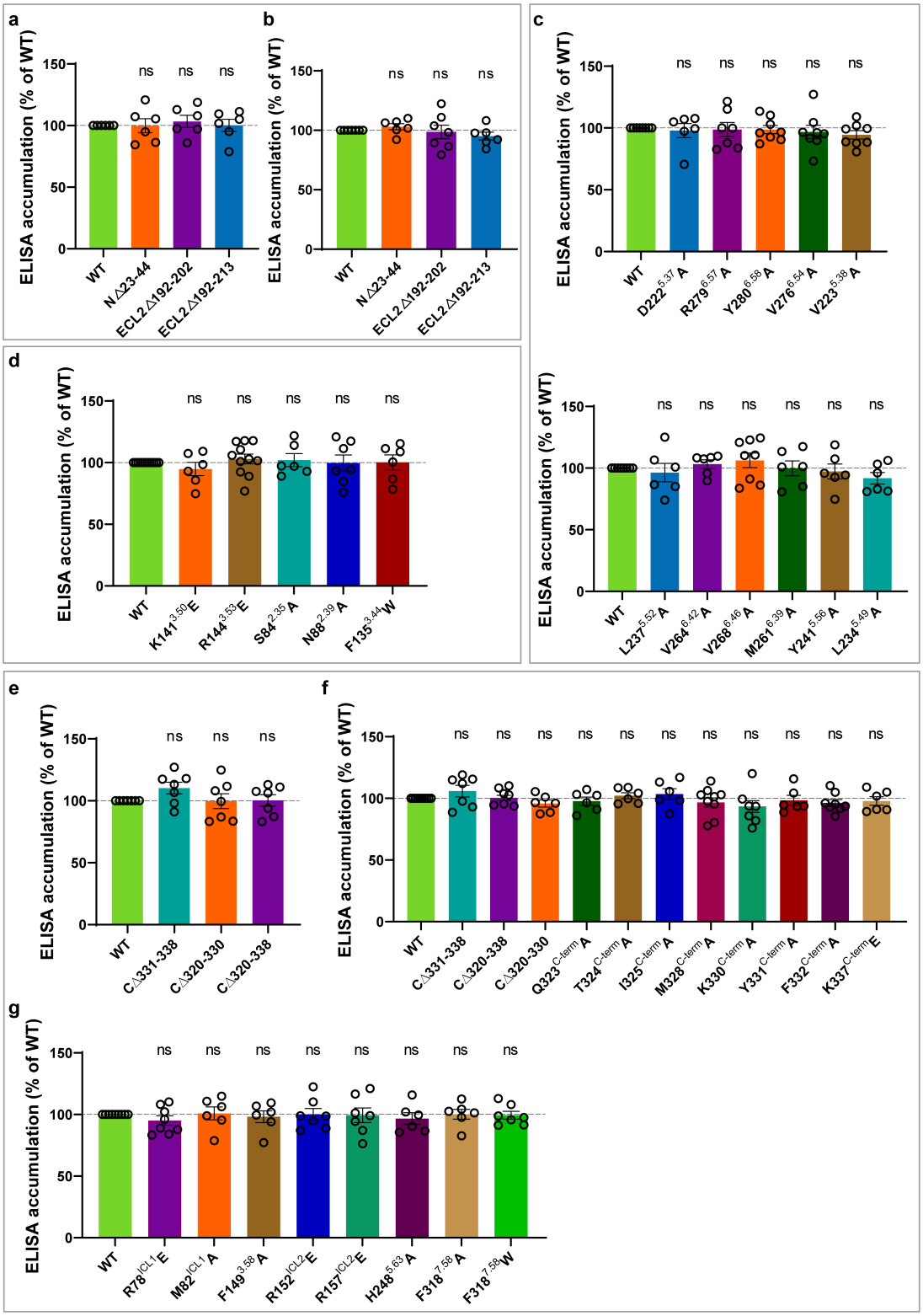

Supplementary Fig. 7 | Surface expression profiles of GPR156 mutants, related to Figs. 3, 4, 5, and 6.

a, b, Surface expression of WT and three constructs with mutations in the N-terminus and ECL2 of GPR156 in the BRET-based assay (**a**) (from left to right $n = 6, 6, 6$; NΔ23-44 vs WT: P=0.9823; Δ192-202 vs WT: P=0.5129; Δ192-213 vs WT:

P=0.9619) and NanoBiT-based assay (**b**) (from left to right *n* = 6, 7, 6; NΔ23-44 vs WT: *P*=0.2373; Δ192-202 vs WT: *P*=0.8155; Δ192-213 vs WT: *P*=0.1402), related to **Fig. 3d, e**, respectively. **c,** Surface expression of WT and mutant constructs with mutations in the transmembrane interface of GPR156 in the BRET-based assay (from left to right *n* = 8, 6, 7, 8, 8, 8, 8, 6, 6, 8, 6, 6, 6; D222$^{5.37}$A vs WT: *P*=0.6641; R279$^{6.57}$A vs WT: *P*=0.8154; Y280$^{6.58}$A vs WT: *P*=0.7103; V276$^{6.54}$A vs WT: *P*=0.5593; V223$^{5.38}$A vs WT: *P*=0.1163; L237$^{5.52}$A vs WT: *P*=0.5763; V264$^{6.42}$A vs WT: *P*=0.2896; V268$^{6.46}$A vs WT: *P*=0.3137; M261$^{6.39}$A vs WT: *P*=0.9733; Y241$^{5.56}$A vs WT: *P*=0.6069; L234$^{5.49}$A vs WT: *P*=0.0625), related to **Fig. 4e**. **d,** Surface expression of WT and mutant constructs with mutations in the TMD of GPR156 in the BRET-based assay (from left to right *n* = 7, 7, 7, 7; K141$^{3.50}$E vs WT: *P*=0.1761; R144$^{3.53}$E vs WT: *P*=0.4340; S84$^{2.35}$A vs WT: *P*=0.5774； N88$^{2.39}$A vs WT: *P*=0.9523; F135$^{3.44}$W vs WT: *P*=0.9509), related to **Fig. 5d**. **e,** Surface expression of WT and mutant versions of the C-terminal tail of GPR156 in the NanoBiT-based assay (from left to right *n* = 12, 6, 11, 6, 7, 6; CΔ331-338 vs WT: *P*=0.0505; CΔ320-330 vs WT: *P*=0.9590; CΔ320-338 vs WT: *P*=0.9474), related to **Fig. 6f**. **f,** Surface expression of WT and mutant versions of the C-terminal tail of GPR156 in the BRET-based assay (from left to right *n* = 10, 7, 6, 7, 6, 6, 6, 9, 7, 6, 8, 6; CΔ331-338 vs WT: *P*=0.1471; CΔ320-330 vs WT: *P*=0.0734; CΔ320-338 vs WT: *P*=0.5272; Q323$^{C\text{-term}}$A vs WT: *P*=0.3773; T324$^{C\text{-term}}$A vs WT: *P*=0.2654; I325$^{C\text{-term}}$A vs WT: *P*=0.3266; M328$^{C\text{-term}}$A vs WT: *P*=0.5332; K330$^{C\text{-term}}$A vs WT: *P*=0.1361; Y331$^{C\text{-term}}$A vs WT: *P*=0.6206; F332$^{C\text{-term}}$A vs WT: *P*=0.1515; K337$^{C\text{-term}}$E vs WT: *P*=0.4299), related to **Fig. 6g**. **g,** Surface expression of WT and mutant constructs of the seven key residues in the BRET-based assay (from left to right *n* = 9, 8, 6, 6, 7, 7, 6, 6, 7; R78^{ICL1}E vs WT: *P*=0.1892; M82^{ICL1}A vs WT: *P*=0.8462; F149$^{3.58}$A vs WT: *P*=0.6400; R152^{ICL2}E vs WT: *P*=0.9768; R157^{ICL2}E vs WT: *P*=0.9065; H248$^{5.63}$A vs WT: *P*=0.3957; F318$^{7.58}$A vs WT: *P*=0.9565; F318$^{7.58}$W vs WT: *P*=0.8343), related to **Fig. 6h**. All of which were measured by ELISA assay. Data are presented as the percentage of WT activity and are shown as the mean ± SEM (bars) from at least six independent experiments performed in technical triplicates with individual data points shown (dots). ns (not significant) = $P > 0.05$, *$P < 0.05$, **$P < 0.01$, ***$P < 0.001$, ****$P < 0.0001$ by two-tailed unpaired t-test compared to WT. **Supplementary Tables 3 and 4** provide detailed information. Source data are provided as a Source Data file.

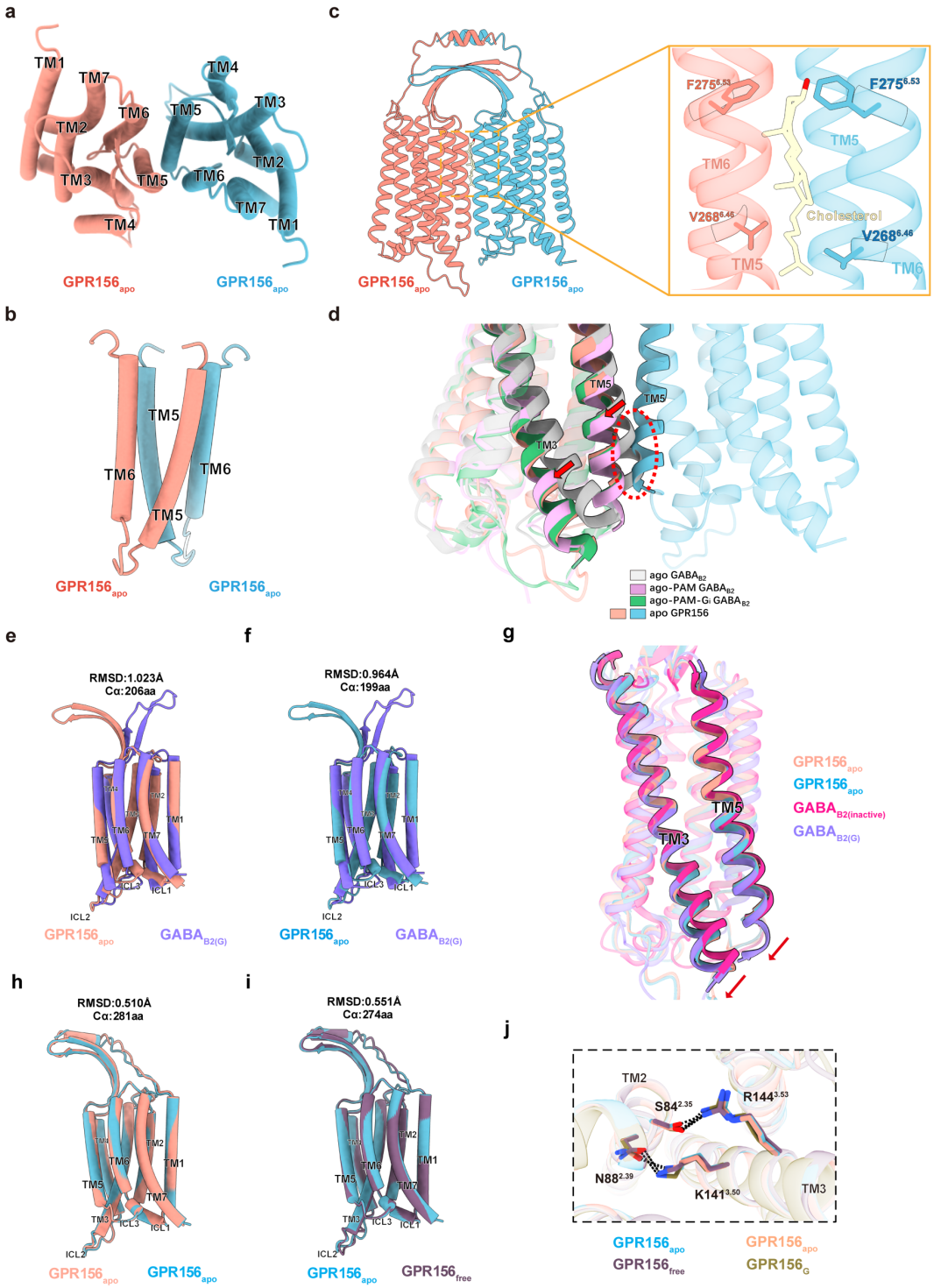

Supplementary Fig. 8 | Conformational comparisons of apo GPR156 with other class C GPCRs.

a, b, Overall arrangement of the TM5/6 domains of the GPR156 homodimer is shown as a top (**a**) and side view (**b**). **c,** The orthogonal view of the 7TM dimer interface with the cholesterol molecule in $GPR156_{apo}$–$GPR156_{apo}$, and detailed interactions in this region in which cholesterol mediates the interaction between TM5 and TM6 of the 7TM protomers. **d,** Structural comparisons of apo GPR156 with the agonist-bound $GABA_B$ (ago) (PDB code: 6UO9), agonist and PAM-bound $GABA_B$ (ago/PAM)

(PDB code: 6UO8), and G_i-bound $GABA_B$ (ago/PAM–G_i) (PDB code: 7EB2). **e, f,** Comparison of the TMD of two apo GPR156 subunits and $GABA_{B2(G)}$ (PDB code: 7EB2), separately (**e, f**). The RMSD levels were calculated. **g,** Side views of the superposed structures of the two $GPR156_{apo}$, $GABA_{B2(G)}$ (PDB code: 7EB2), and $GABA_{B2(inactive)}$ (PDB code: 6WIV) aligned to the TMD of $GABA_{B2(G)}$. TM3 and TM5 are highlighted. **h, i,** Comparison of the two protomers of apo GRP156 (**h**), apo GPR156 and the GPR156 G-free subunit (**i**). The RMSD levels were calculated. **j,** Magnified views of the detailed interactions within the TMD of each protomer from apo GPR156 and G_i-bound GRP156 complex.

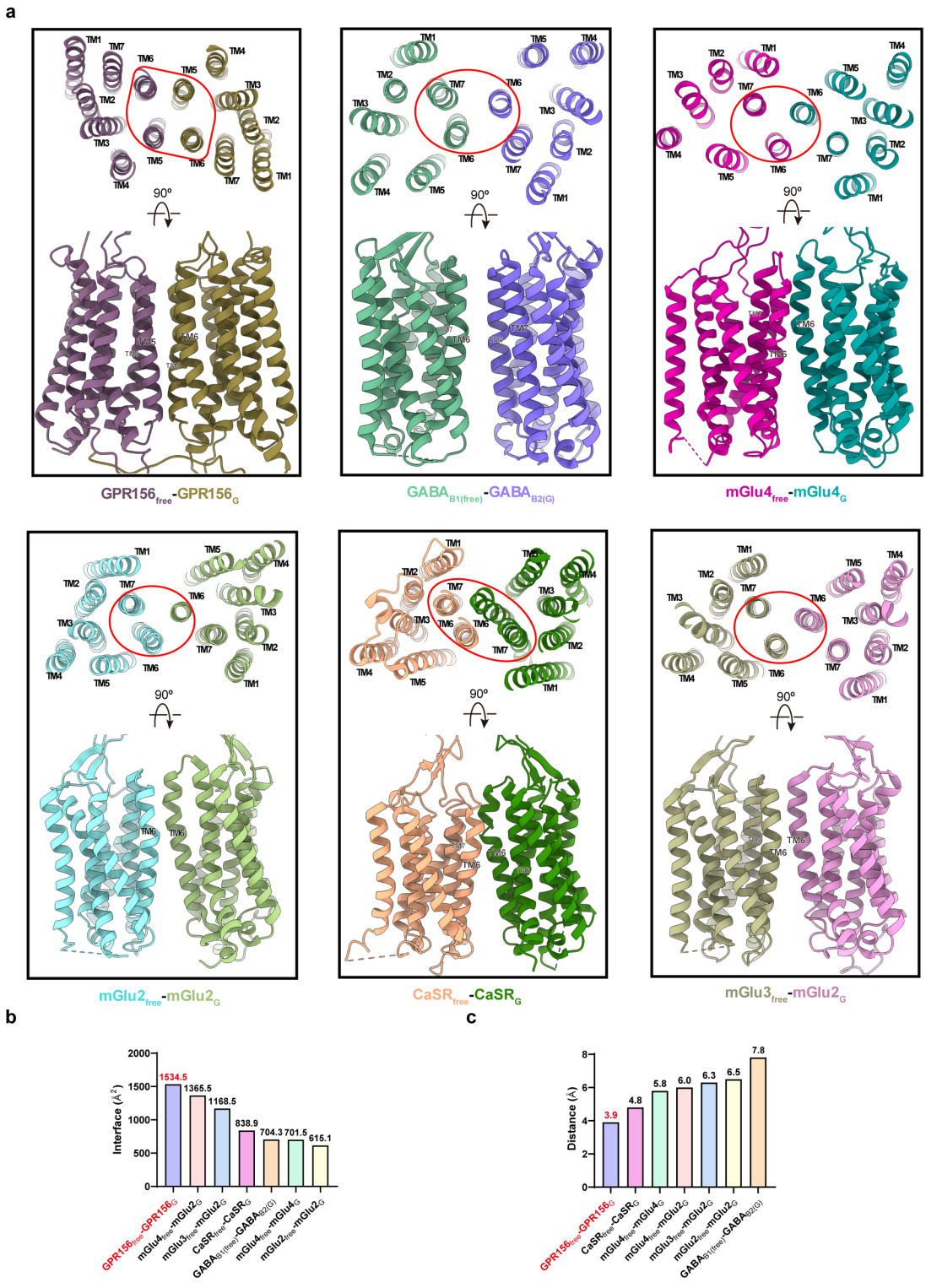

Supplementary Fig. 9 | Comparison of the transmembrane dimer interface of GPR156 with other class C GPCR–G complexes.

a, Comparison of 7TM dimerization with G protein across class C GPCRs, including GPR156, $GABA_{B1(free)}$–$GABA_{B2(G)}$ (PDB code: 7EB2), $mGlu4_{free}$–$mGlu4_G$ (PDB code: 7E9H), $mGlu2_{free}$–$mGlu2_G$ (PDB code: 7MTS), $CaSR_{free}$–$CaSR_G$ (PDB code: 8WPU), and $mGlu3_{free}$–$mGlu2_G$ (PDB code: 8JD3). **b, c,** Statistical analysis of the dimeric interface area (**b**) and the distance (**c**) of class C GPCR dimers with the G protein

(including $GPR156_{free}$–$GPR156_G$ (Cα of G244-G244), $CaSR_{free}$–$CaSR_G$ (Cα of T828-A824; PDB code: 8WPU), $mGlu4_{free}$–$mGlu4_G$ (Cα of I804-I804; PDB code: 7E9H), $mGlu4_{free}$–$mGlu2_G$ (Cα of T808-V782; PDB code: 8JD5), $mGlu3_{free}$–$mGlu2_G$ (Cα of T792-V782; PDB code: 8JD3), $mGlu2_{free}$–$mGlu2_G$ (Cα of T783-V782; PDB code: 7MTS), and $GABA_{B1(free)}$–$GABA_{B2(G)}$ (Cα of A832-L712; PDB code: 7EB2)). Source data are provided as a Source Data file.

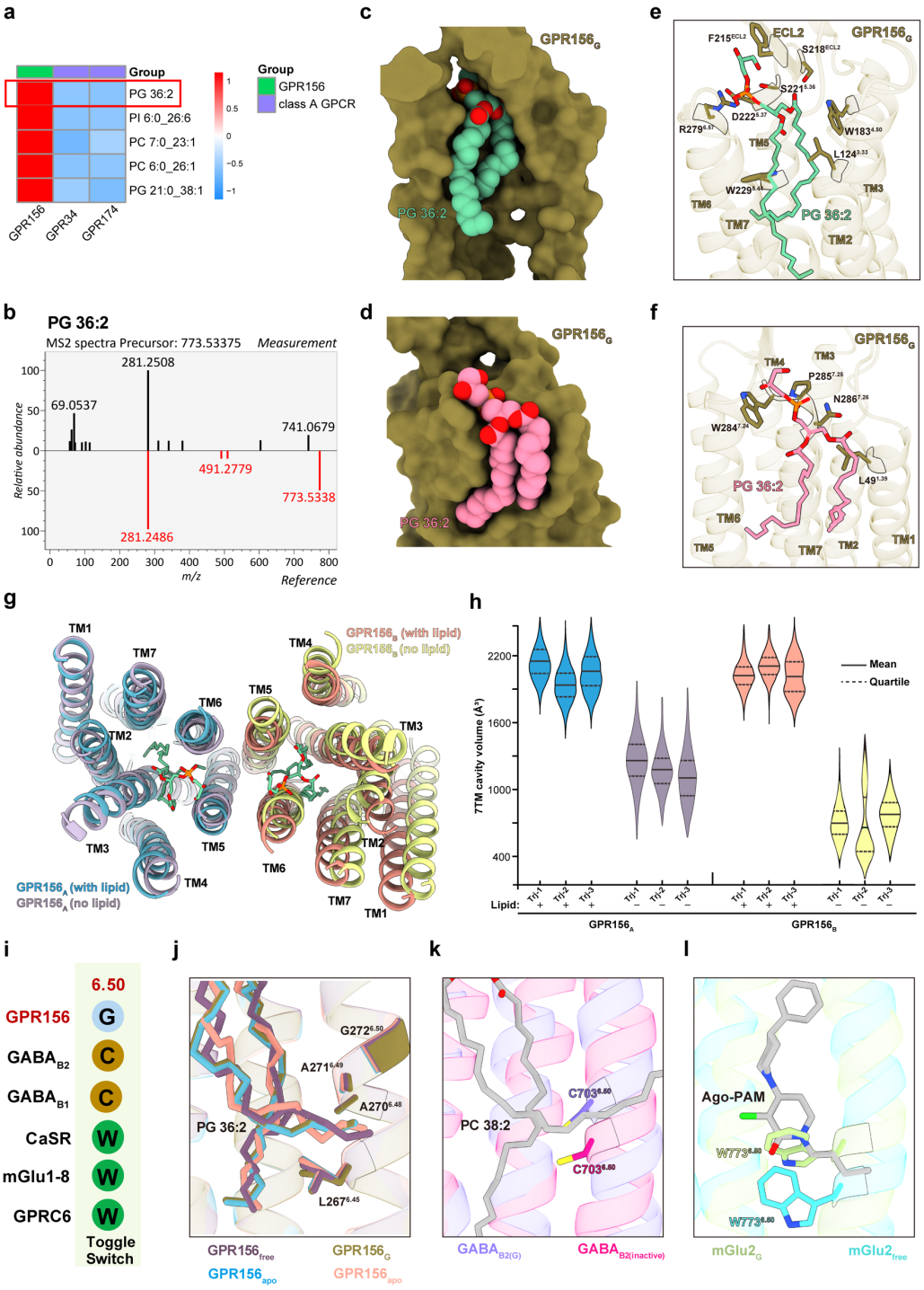

Supplementary Fig. 10 | Identification of the endogenous lipid molecule in the structures of GPR156.

a, Heatmap visualization of the differential enrichment of phospholipids derived from LC-MS/MS analysis of samples from GPR156 (n = 3) and two other class A GPCRs (GPR34 and GPR174) (n for GPR34= 2, n for GPR174= 2) that do not contain phospholipids in their known structures. Source data are provided as a Source Data file. **b,** High-resolution MS2 spectra of the peak (black) matched with standard spectra of PG 36:2 in red. **c-f,** The maps were compared (**c, d**), and the LC-MS/MS results led to the decision to model PG 36:2 in the pocket within the $GPR156_G$

subunits (**e**) and located at the extrahelical site (**f**). **g,** Representative top view of the GPR156-dimer cartoon model from the three replicates of MD simulations at 300 ns. **h,** The collapse of the transmembrane cavity in the three replicates when phospholipids were removed (as assessed by the 7TM cavity volume), refer to **Supplementary Fig. 12** for details. **i,** The key residue in the toggle switch motif (6.50) was aligned among members of class C GPCRs. **j-l,** Close-up view of the conserved toggle switch motif in GPR156 (**j**) and other members of the class C subfamily, including $GABA_B$ receptor (PDB codes: 7EB2 and 6WIV) (**k**) and mGlu2 (PDB code: 7MTS) (**l**). The phospholipids of different GPR156 subunits (PG 36:2) are displayed by the color of the corresponding subunits. Phospholipids in $GABA_B$ receptor (PC 38:2) and ago-PAM in $mGlu2_G$ are marked with gray.

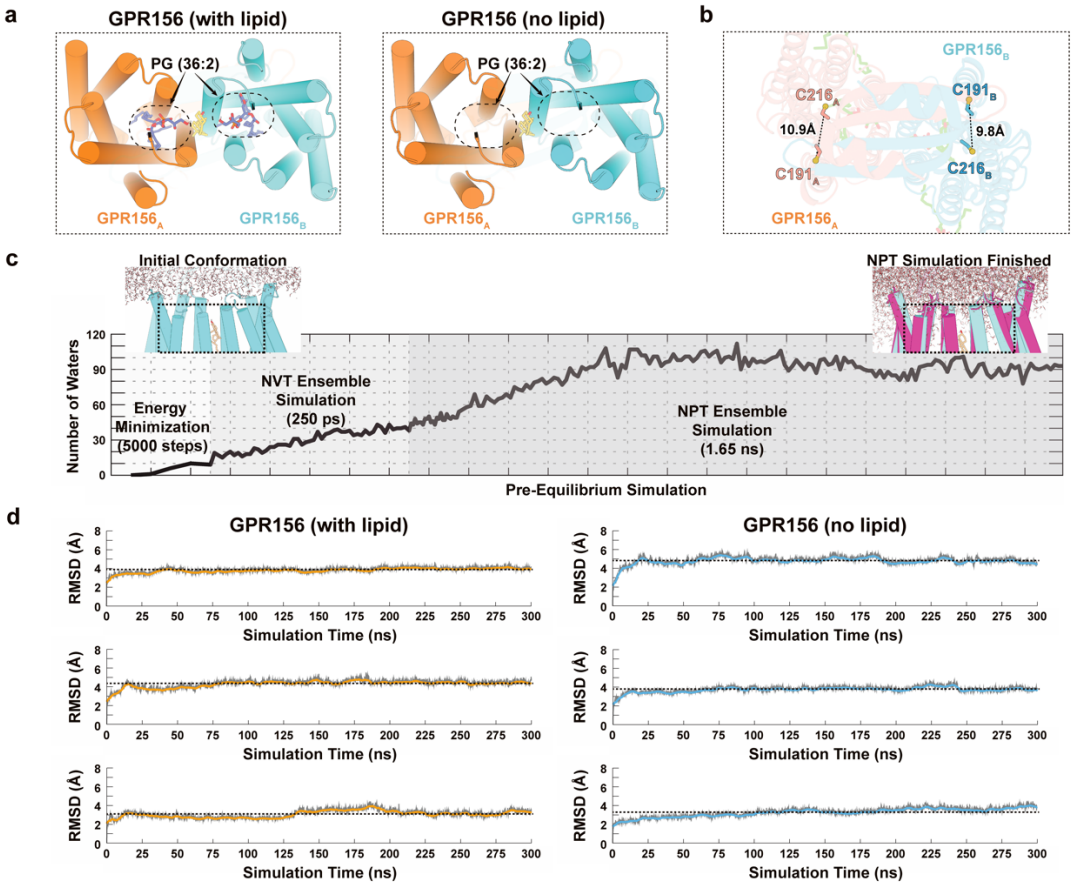

Supplementary Fig. 11 | MD simulation details and stability evaluation.
a, The snapshot of the initial structure for the GPR156 (with lipid) and the GPR156 (no lipid) systems with the endogenous lipid PG (36:2) removed. **b,** The distance between sulfur atoms of C191 and C216 in the GPR156 apo structure. **c,** The number of water molecules that filled in the 7TM cavity of GPR156 (no lipid) system over the pre-equilibrium simulation. **d**, The RMSD of all heavy atoms of GPR156 over the simulation time for both the GPR156 (with lipid) and the GPR156 (no lipid) systems.

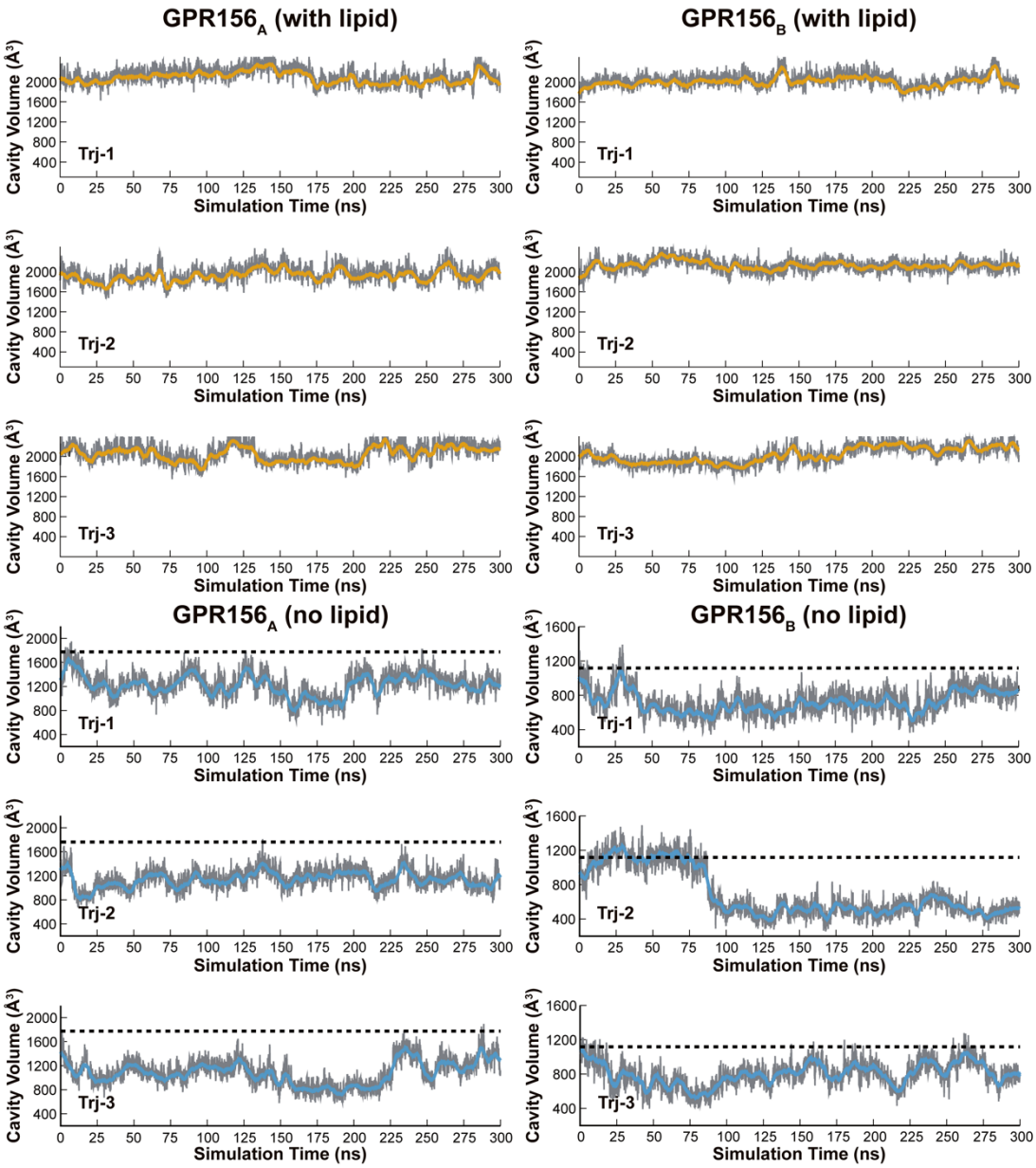

Supplementary Fig. 12 | The volume of phospholipid-bound 7TM cavity was measured over time for individual simulations.

The volume of phospholipid-bound 7TM cavity of chain A and chain B measured for the three independent trajectories of the GPR156 (with lipid) and the GPR156 (no lipid) systems separately.

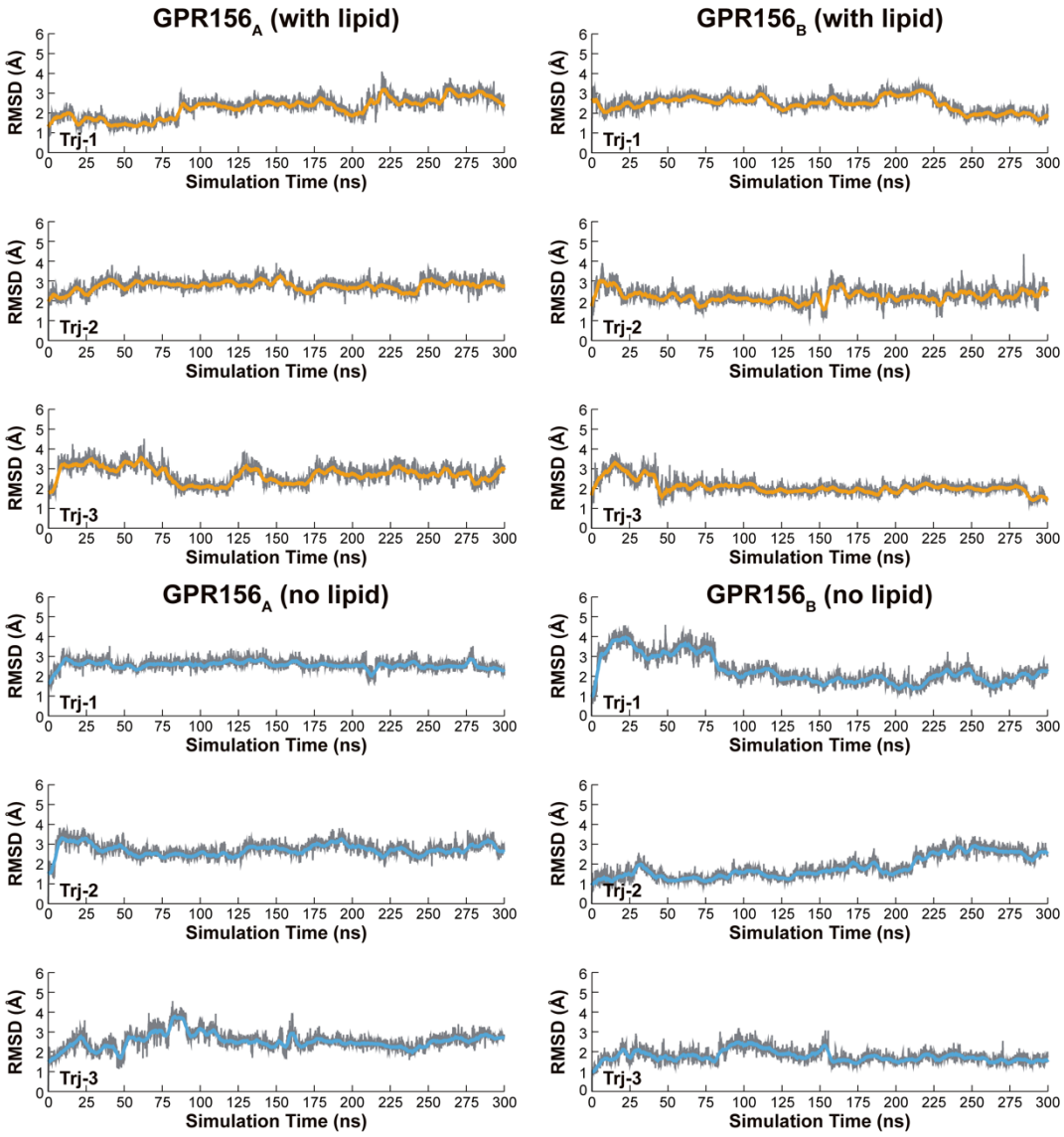

Supplementary Fig. 13 | RMSD of TM3 helix intracellular end measured over time for individual simulations.

The RMSD of TM3 helix intracellular end of chain A and chain B measured for the three independent trajectories of the GPR156 (with lipid) and the GPR156 (no lipid) systems separately.

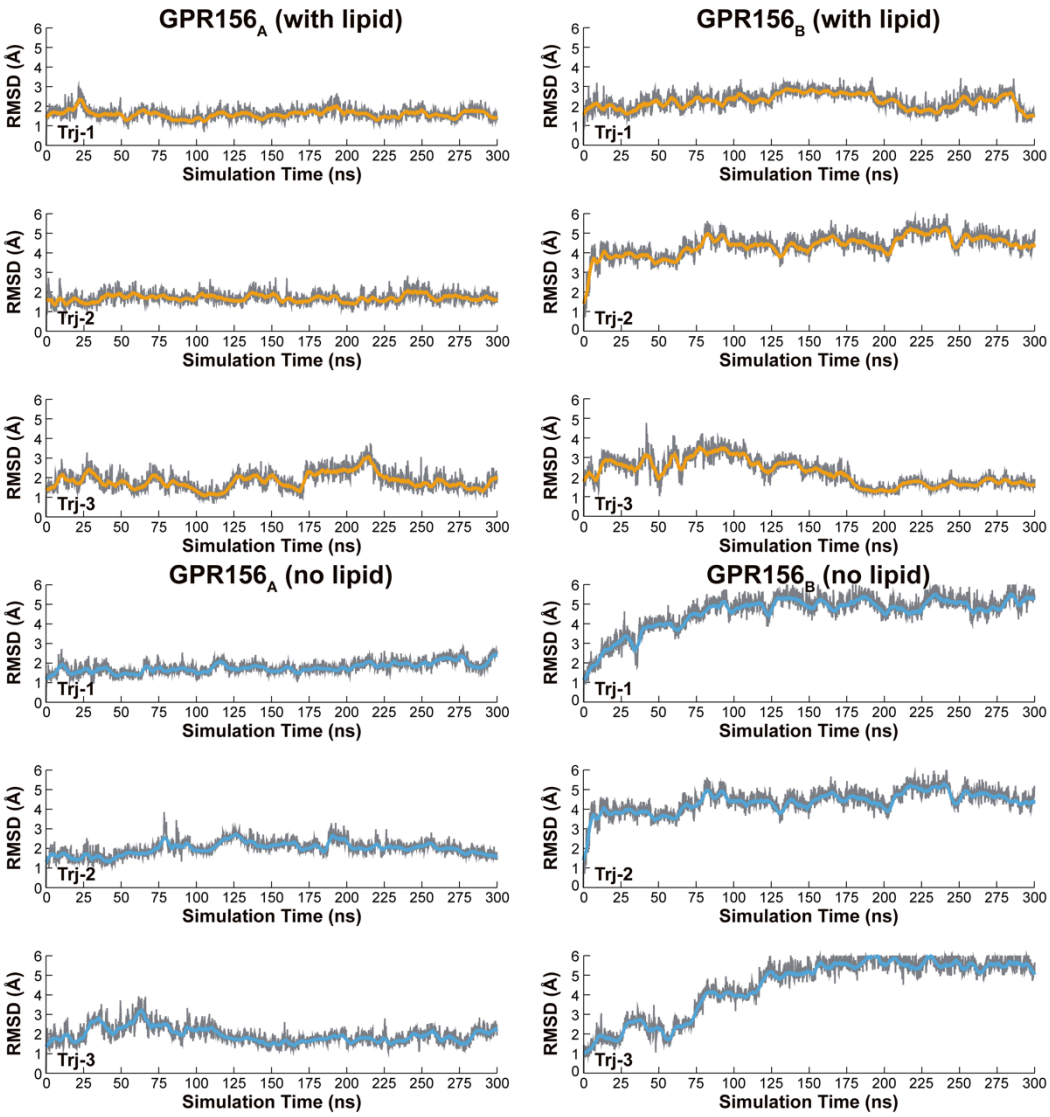

Supplementary Fig. 14 | RMSD of TM5 helix intracellular end measured over time for individual simulations.

The RMSD of TM5 helix intracellular end of chain A and chain B measured for the three independent trajectories of the GPR156 (with lipid) and the GPR156 (no lipid) systems separately.

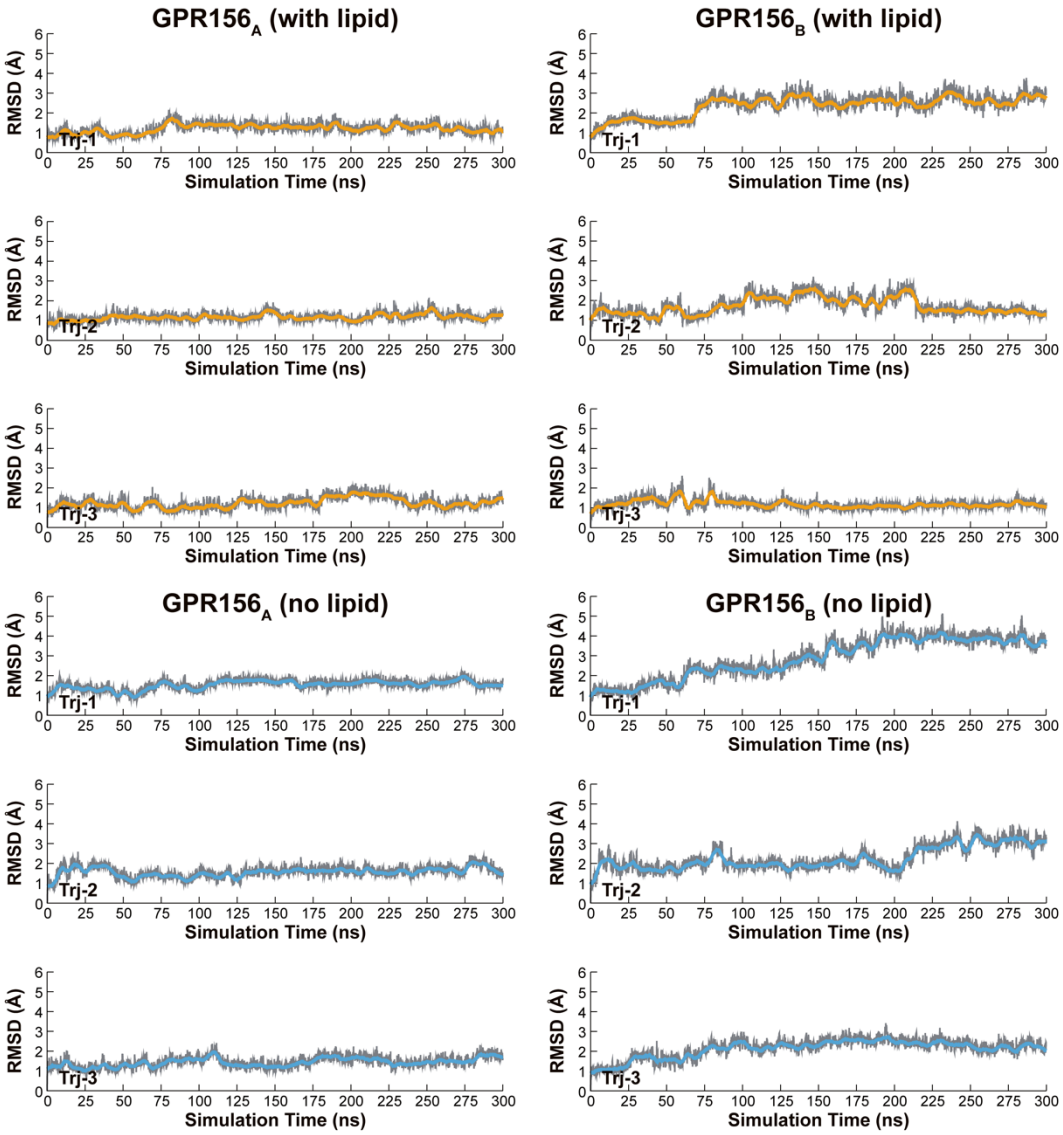

Supplementary Fig. 15 | RMSD of TM6 helix intracellular end measured over time for individual simulations.

The RMSD of TM6 helix intracellular end of chain A and chain B measured for the three independent trajectories of the GPR156 (with lipid) and the GPR156 (no lipid) systems separately.

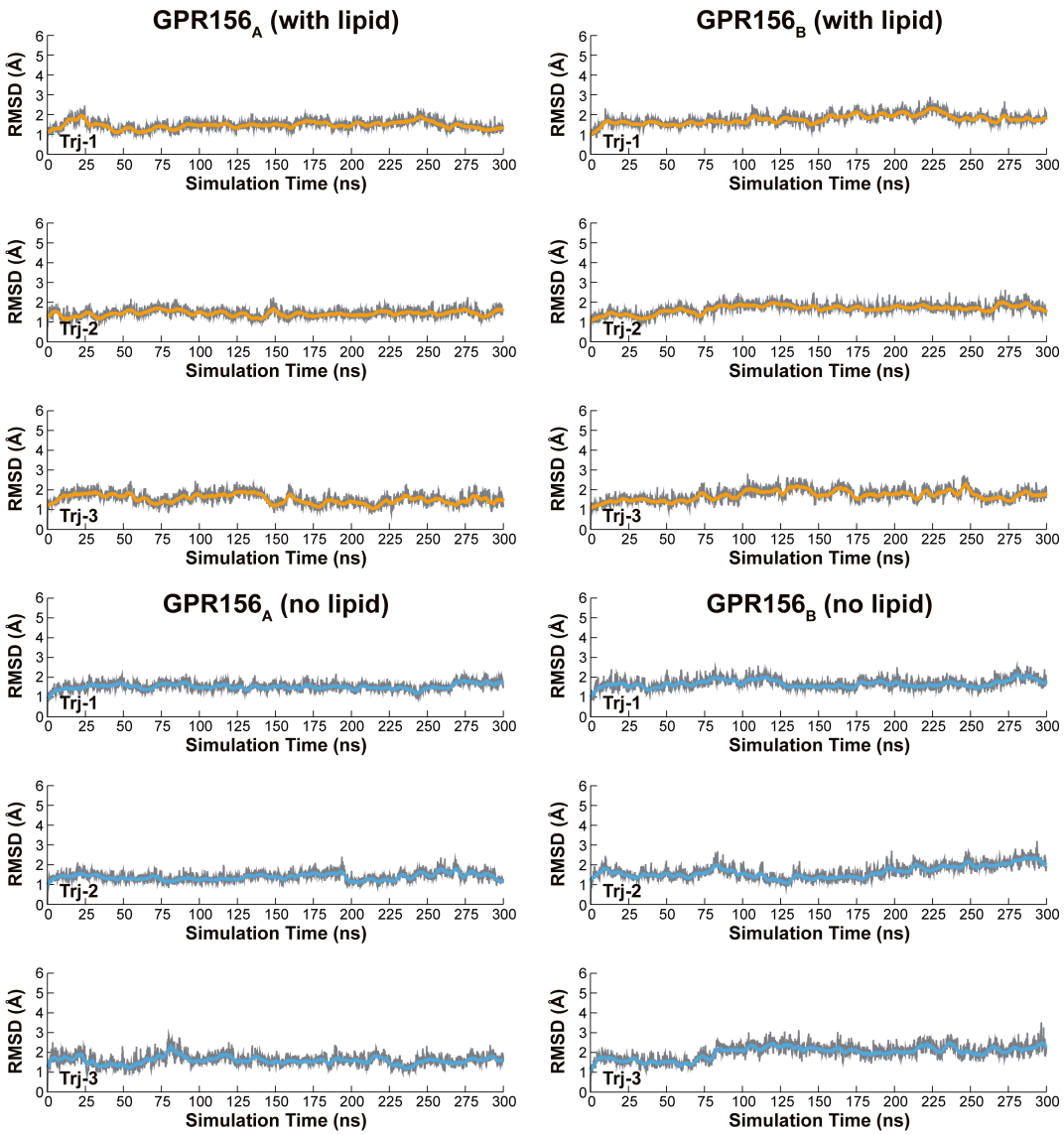

Supplementary Fig. 16 | RMSD of TM7 helix intracellular end measured over time for individual simulations.

The RMSD of TM7 helix intracellular end of chain A and chain B measured for the three independent trajectories of the GPR156 (with lipid) and the GPR156 (no lipid) systems separately.

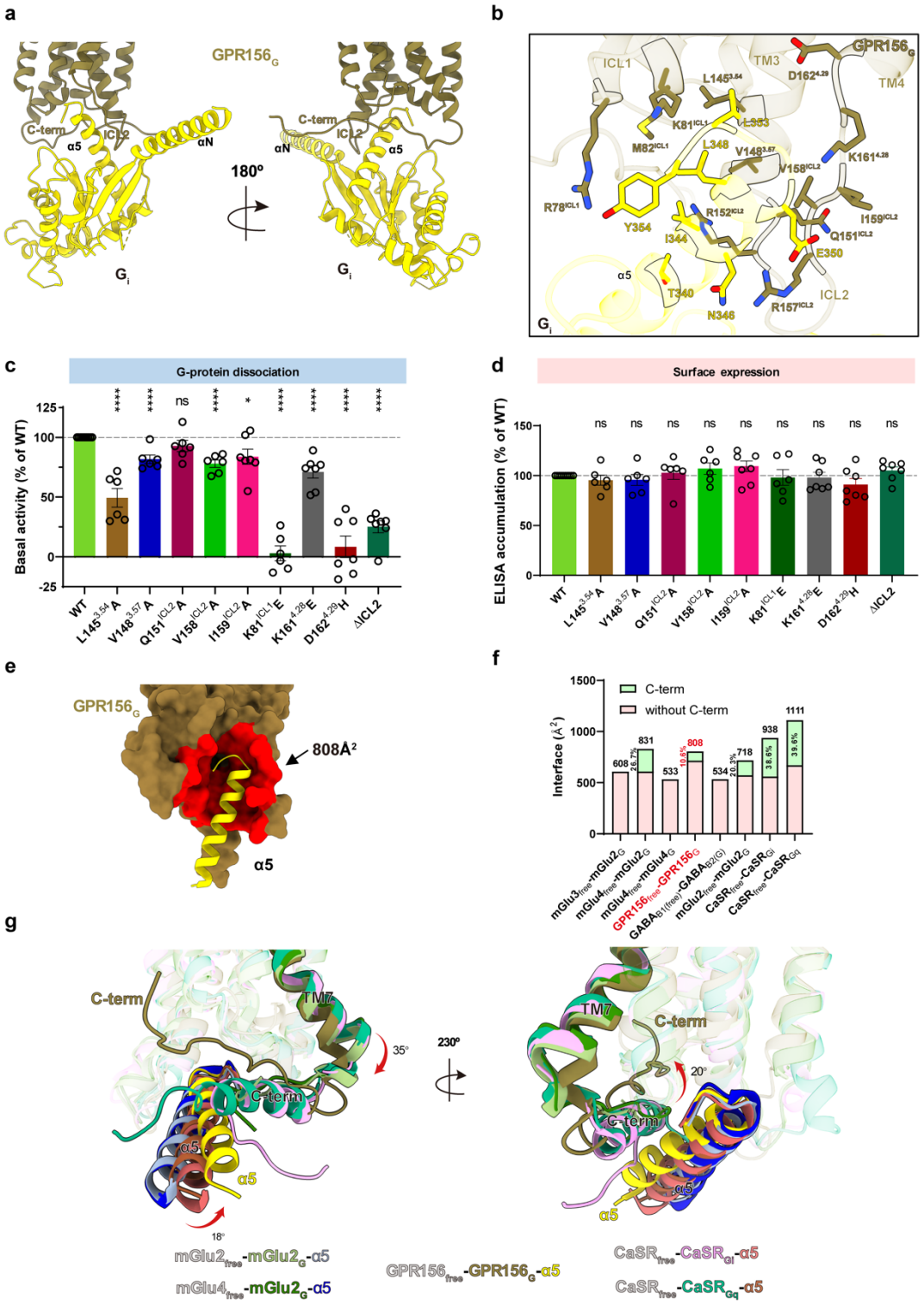

Supplementary Fig. 17 | Comparison of the G_i binding pocket and the C-terminus conformation of GPR156 with other class C GPCRs.

a, The G_{i3} binding pocket in GPR156, which is mainly formed by ICL2, ICL1, and the C-terminus of the G-bound subunit. **b,** Detailed interactions of ICL1, ICL2, TM3, and TM4 of the G-bound subunit with $G\alpha_i$. **c, d,** The basal activity (**c**) (from left to right $n = 9, 6, 6, 6, 6, 7, 6, 7, 7, 7$; $L145^{3.54}A$ vs WT: P=1.9367E-06; $V148^{3.57}A$ vs WT: P=2.3859E-05; $Q151^{ICL2}A$ vs WT: P=0.0778; $V158^{ICL2}A$ vs WT: P=6.1673E-

07; I159^{ICL2}A vs WT: *P*=0.0108; K81^{ICL1}E vs WT: *P*=4.9575E-11; K161$^{4.28}$E vs WT: *P*=1.3239E-05; D162$^{4.29}$H vs WT: *P*=1.4577E-08; ΔICL2 vs WT: *P*=8.0139E-11) and surface expression (**d**) (from left to right *n* = 9, 6, 6, 6, 6, 7, 6, 7, 7, 7; L145$^{3.54}$A vs WT: *P*=0.2783; V148$^{3.57}$A vs WT: *P*=0.3542; Q151^{ICL2}A vs WT: *P*=0.6070; V158^{ICL2}A vs WT: *P*=0.1459; I159^{ICL2}A vs WT: *P*=0.1551; K81^{ICL1}E vs WT: *P*=0.7657; K161$^{4.28}$E vs WT: *P*=0.6815; D162$^{4.29}$H vs WT: *P*=0.1082; ΔICL2 vs WT: *P*=0.1376) of WT and mutant versions in the G_i binding pocket of GPR156, as measured by the BRET-based assay and ELISA assay, respectively. Data are presented as the percentage of WT activity and are shown as the mean ± SEM (bars) from at least six independent experiments performed in technical triplicate with individual data points shown (dots). ns (not significant) = $P > 0.05$, *$P < 0.05$, **$P < 0.01$, ***$P < 0.001$, ****$P < 0.0001$ by two-tailed unpaired t-test compared to WT. **Supplementary Table 3** provides detailed information. **e,** Interface of GPR156 and the G_{i3} protein. The interaction interface between GPR156 and α5 of $G\alpha_i$ is in red. Source data are provided as a Source Data file. **f,** Statistical diagram of the G-protein interaction area of class C GPCR dimers. The C-terminus's contribution is shown in green. Source data are provided as a Source Data file. **g,** Comparisons of the C-terminus and the α5 of $G\alpha_i$ between the GPR156 and $mGlu2_{free}$–$mGlu2_G$ (PDB code: 7MTS), $mGlu4_{free}$–$mGlu2_G$ (PDB code: 8JD5), $CaSR_{free}$–$CaSR_{Gi}$ (PDB code: 8SZH), and $CaSR_{free}$–$CaSR_{Gq}$ (PDB code: 8SZG). The four structures were aligned by the G-bound subunit of the GPR156 TMD as the reference.

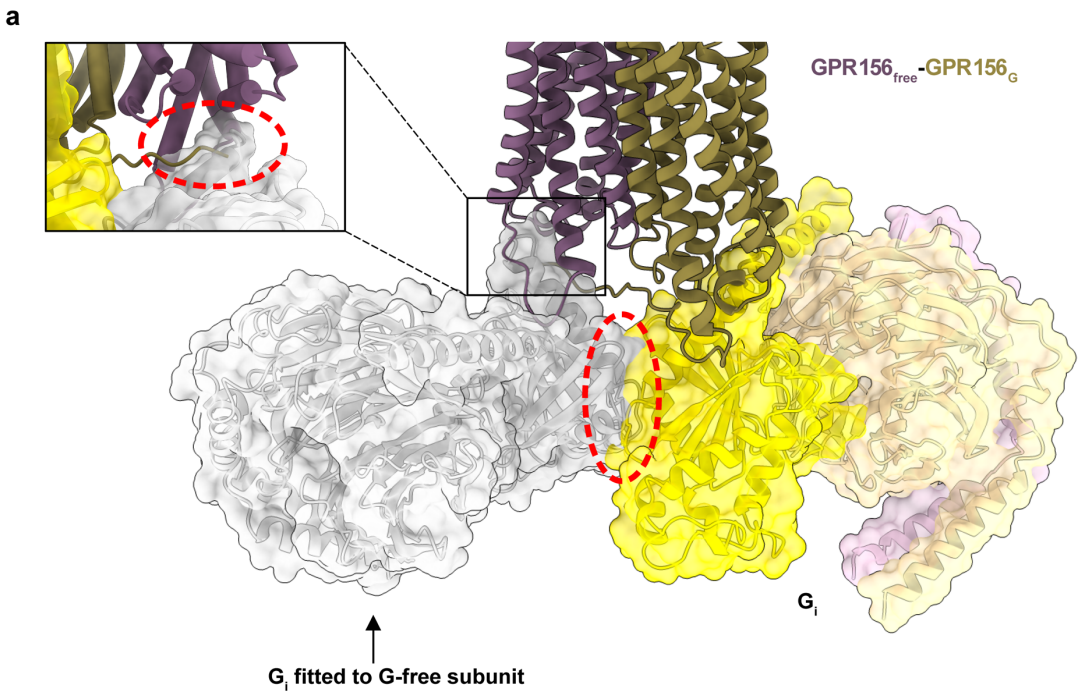

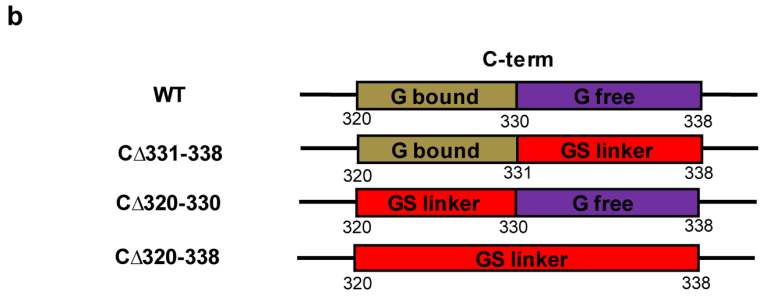

Supplementary Fig. 18 | Diagram illustrating steric hindrance when simultaneous coupling to two G proteins and the design of the C-terminal truncation constructs.

a, Two kinds of steric hindrance prevent both GPR156 protomers from being activated by the G_i-protein heterotrimer. **b,** Diagram of WT GPR156's C-terminus compared to the mutant constructs that were substituted with a GS link (CΔ331–338, CΔ320–330, and CΔ320–338). GS link: A linker composed of glycine and serine.

Supplementary Table 1 | Basal activity of the primary structure (FL) and the purification construct (EM) of GPR156, as measured by BRET and ELISA accumulation assay.

Mutants	ΔBRET			Expression	
	% of FL	*P* value	*n*	% of FL	*P* value
FL	100	/	6	100	/
EM	94.69±3.06	0.1131	6	94.41±3.26	0.1173

Data are mean ± SEM from at least six independent experiments. ns (not significant) = $P > 0.05$, *$P < 0.05$, **$P < 0.01$, ***$P < 0.001$, ****$P < 0.0001$ by two-tailed unpaired t-test compared to the response of wild type.

Supplementary Table 2 | Cryo-EM data collection, refinement, and validation statistics.

	apo GPR156	GPR156-G_{i3} complex
Data collection and processing		
Magnification	150,540	150,540
Voltage (kV)	300	300
Electron exposure (e^{-}/Å^2)	52	52
Defocus range (μm)	-1.0 ~ -2.5	-1.0 ~ -2.5
Pixel size (Å)	0.93	0.93
Symmetry imposed	C2	C1
Initial particle projections (no.)	17,010,572	12,058,641
Final particle projections (no.)	329,646	1,153,971
Map resolution (Å)	3.09	2.39
FSC threshold	0.143	0.143
Map resolution range (Å)	2.0-5.0	2.0-3.0
Refinement		
Initial model used	AlphaFold2	AlphaFold2 & 7E9H
Model resolution (Å)	3.5	3.3
FSC threshold	0.5	0.5
Model resolution range (Å)	1.5-3.5	2.0-3.3
Map sharpening *B* factor (Å^2)	DeepEMhancer	DeepEMhancer
Model composition		
Non-hydrogen atoms	4,946	9,831
Protein residues	596	1232
B factors (Å^2)		
Protein	56.72	113.73
Ligand	34.29	48.52
R.m.s. deviations		
Bond lengths (Å)	0.021	0.018
Bond angles (°)	0.879	0.947
Validation		
MolProbity score	2.02	2.03
Clashscore	15.46	16.17
Rotamer outliers (%)	0.00	0.00
Ramachandran plot		
Favored (%)	95.27	95.40
Allowed (%)	4.73	4.60
Disallowed (%)	0.00	0.00

Supplementary Table 3 | Basal activity of wild-type GPR156 and mutants, as measured by the BRET and ELISA accumulation assays.

	Mutants	ΔBRET			Expression	
		% of WT	*P* value	*n*	% of WT	*P* value
	WT	100	/	12	100	/
Extracellular region	NΔ23-44	110.6±3.71	0.0170	6	99.87±5.68	0.9823
	Δ192-213	91.88±4.76	0.1190	6	100.2±4.89	0.9619
	Δ192-202	98.77±4.60	0.7947	6	103.4±4.94	0.5129
Active state feature	$K141^{3.50}E$	45.36±3.49	3.9825E-11	6	94.80±3.67	0.1761
	$R144^{3.53}E$	19.45±6.00	8.9060E-12	11	103.0±3.76	0.4340
	$S84^{2.35}A$	89.83±3.40	0.0086	6	102.1±3.61	0.5774
	$N88^{2.39}A$	100.4±3.45	0.9080	7	99.71±4.84	0.9523
	$F135^{3.44}W$	70.56±3.35	1.5807E-07	6	100.3±4.11	0.9509
G_{i3} binding pocket	$L145^{3.54}A$	49.32±6.25	1.9367E-06	6	95.45±4.02	0.2783
	$V148^{3.57}A$	81.65±2.87	2.3859E-05	6	95.76±4.42	0.3542
	$Q151^{ICL2}A$	92.71±3.81	0.0778	6	102.8±5.26	0.6070
	$V158^{ICL2}A$	77.92±2.46	6.1673E-07	6	107.0±4.55	0.1459
	$I159^{ICL2}A$	83.79±5.52	0.0108	7	107.5±4.98	0.1551
	$K81^{ICL1}E$	2.90±4.96	4.9575E-11	6	98.10±6.25	0.7657
	$K161^{4.28}E$	71.01±4.44	1.3239E-05	7	98.08±4.57	0.6815
	$D162^{4.29}H$	8.335±7.91	1.4577E-08	7	91.08±5.20	0.1082
	ΔICL2	25.06±4.35	8.0139E-11	7	105.0±3.18	0.1376
Dimer interface I	$D222^{5.37}A$	74.25±3.10	2.5282E-06	6	97.83±4.87	0.6641
	$R279^{6.57}A$	103.3±5.62	0.5694	7	98.72±5.35	0.8154
	$Y280^{6.58}A$	90.97±4.34	0.0560	8	98.74±3.33	0.7103
	$V276^{6.54}A$	85.32±5.07	0.0118	8	96.78±5.38	0.5593
	$V223^{5.38}A$	73.20±6.13	0.0006	8	94.42±3.33	0.1163
Dimer interface II	$L237^{5.52}A$	61.19±3.26	5.2657E-08	6	96.35±6.36	0.5763
	$V264^{6.42}A$	81.27±4.60	0.0015	6	103.2±2.92	0.2896
	$V268^{6.46}A$	85.63±5.99	0.0309	8	106.2±5.96	0.3137
	$M261^{6.39}A$	70.81±2.88	3.1286E-07	6	99.82±5.13	0.9733
	$Y241^{5.56}A$	78.48±5.21	0.0014	6	97.26±5.20	0.6069
	$L234^{5.49}A$	72.43±3.64	6.6258E-06	6	91.78±4.01	0.0625
C-terminal tail	CΔ331-338	58.70±3.38	7.4009E-09	7	105.9±3.85	0.1471
	CΔ320-330	20.00±7.24	5.5541E-08	6	95.82±2.16	0.0734
	CΔ320-338	14.63±6.73	4.6108E-09	7	101.4±2.09	0.5272
	$Q323^{C\text{-}term}A$	32.67±4.92	4.2212E-09	6	97.74±2.48	0.3773
	$T324^{C\text{-}term}A$	119.7±5.00	0.0017	6	102.1±1.84	0.2654
	$I325^{C\text{-}term}A$	108.1±3.70	0.0470	6	103.4±3.34	0.3266
	$M328^{C\text{-}term}A$	76.06±5.00	0.0002	9	97.64±3.71	0.5332
	$K330^{C\text{-}term}A$	65.01±3.90	3.4903E-07	7	92.95±4.48	0.1361
	$Y331^{C\text{-}term}A$	68.75±3.13	1.8316E-07	6	98.45±3.06	0.6206
	$F332^{C\text{-}term}A$	73.21±5.29	0.0001	8	96.31±2.45	0.1515
	$K337^{C\text{-}term}E$	66.96±3.12	9.1879E-08	6	97.87±2.62	0.4299
Key residues related to C-terminal tail	$R78^{ICL1}E$	46.25±3.74	3.5544E-10	8	95.12±3.55	0.1892
	$M82^{ICL1}A$	68.15±3.23	2.1033E-07	6	100.8±4.23	0.8462
	$F149^{3.58}A$	9.62±4.53	3.9032E-11	6	98.18±3.80	0.6400
	$R152^{ICL2}E$	67.05±2.84	1.4385E-08	7	100.1±4.12	0.9768
	$R157^{ICL2}E$	27.21±7.12	7.0588E-08	7	99.38±5.17	0.9065
	$H248^{5.63}A$	64.24±3.80	3.5652E-07	6	96.68±3.78	0.3957
	$F318^{7.58}A$	76.02±3.43	9.5730E-06	6	100.2±3.23	0.9565
	$F318^{7.58}W$	73.22±2.97	3.2740E-07	7	99.43±2.69	0.8343

Data are mean ± SEM from at least six independent experiments. ns (not significant) = $P > 0.05$, *$P < 0.05$, **$P < 0.01$, ***$P < 0.001$, ****$P < 0.0001$ by two-tailed unpaired t-test compared to the response of wild type.

Supplementary Table 4 | Basal activity of wild-type GPR156 and mutants, as measured by the NanoBiT and ELISA accumulation assays.

	Mutants	NanoBiT accumulation			Expression	
		% of WT	*P* value	*n*	% of WT	*P* value
	WT	100	/	7	100	/
C-terminal tail	CΔ331-338	64.50±5.35	2.4064E-05	7	110.2±4.70	0.0505
	CΔ320-330	54.77±4.32	2.1818E-07	7	99.68±6.04	0.9590
	CΔ320-338	38.52±5.47	9.9574E-08	7	100.3±4.57	0.9474
Extracellular region	Δ192-213	93.78±4.36	0.1819	6	95.11±3.08	0.1402
	Δ192-202	99.04±5.74	0.8694	7	98.65±5.66	0.8155
	NΔ23-44	107.5±4.20	0.1038	6	103.0±2.39	0.2373

Data are mean ± SEM from at least six independent experiments. ns (not significant) = $P > 0.05$, *$P < 0.05$, **$P < 0.01$, ***$P < 0.001$, ****$P < 0.0001$ by two-tailed unpaired t-test compared to the response of wild type.

Supplementary Table 5 | Details of the all-atomistic molecular dynamic simulations.

System Name		GPR156 (with lipid)	GPR156 (no lipid)
System size		13.4×13.4×13.1 nm^3	13.4×13.4×13.1 nm^3
Number of lipids (From apo structure)	PG (36:2)	4	2
	Cholesterol	1	1
Number of lipids (Added by CHARMM-GUI)	POPC	180	180
	POPE	60	60
	Cholesterol	7	7
Number of Waters		49,631	49,612
Ions	Na^+	135	134
	Cl^-	154	155

Supplementary Table 6 | RMSD of the transmembrane helix ends in the intracellular side.

RMSD of TM Helix Ends (Å)	$GPR156_A$		$GPR156_B$	
	With lipid	No lipid	With lipid	No lipid
TM3	2.62 ± 0.45	2.65 ± 0.36	2.29 ± 0.40	2.02 ± 0.56
TM5	1.73 ± 0.35	1.94 ± 0.38	2.43 ± 0.62	4.51 ± 0.69
TM6	1.22 ± 0.26	1.53 ± 0.27	1.78 ± 0.42	2.44 ± 0.70
TM7	1.50 ± 0.24	1.53 ± 0.24	1.74 ± 0.28	1.80 ± 0.33

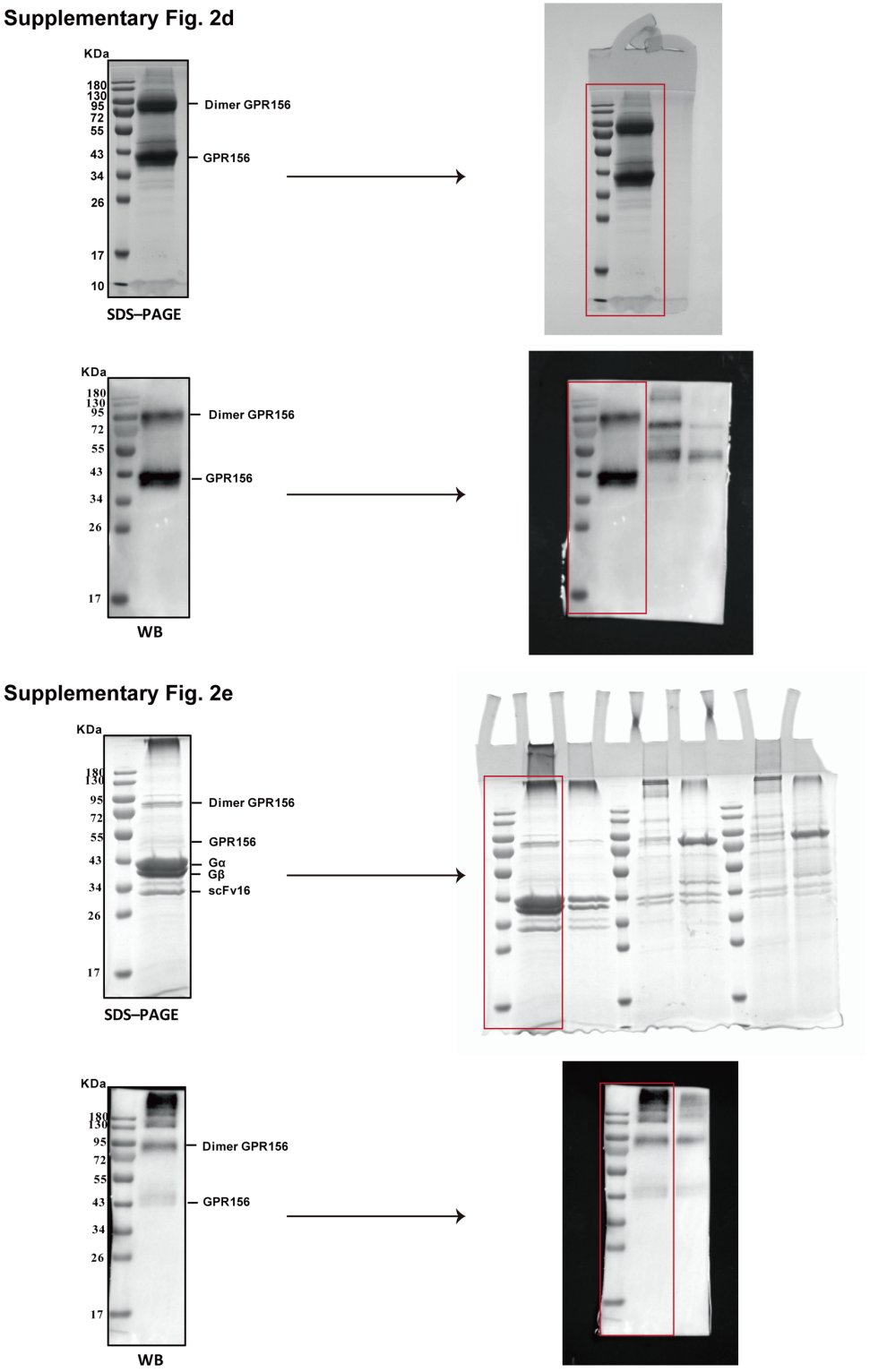

Unprocessed gels and western blots for Supplementary Fig. 2d and e. Cropped regions are indicated as red boxes.